

Polyvalent Interactions of HIV-gp120 Protein and Nanostructures of Carbohydrate Ligands

Jing-Jiang Yu, Birte Nolting, Yih Horng Tan, Xue Li, Jacquelyn Gervay-Hague, and Gang-yu Liu

Department of Chemistry, University of California, Davis, CA 95616, USA

Abstract

This paper presents the initial effort in anti-HIV infection using glycosphingolipid-based nanostructures. HIV infection of CD4 negative cells is initiated by the binding of the viral envelope glycoprotein gp120 to galactosylceramide (GalCer), a glycosphingolipid that serves as the cellular receptor for viral recognition. A series of nanostructures of GalCer are designed and produced using an AFM-based lithography method known as nanografting. The geometry dependence of recombinant gp120 binding to these nanostructures is monitored using high-resolution AFM imaging. Gp120 molecules are found to favor binding sites that allow for polyvalent interactions. Increased adsorption at the intersection of two lines, or between two parallel lines with matching separation for trimeric binding, strongly suggests that trivalent interactions are dominant in gp120–GalCer nanostructure interactions. Systematic distance-dependence studies, using parallel nanolines with various separations, reveal a separation of 4.8 nm, matching the separation of V3 loops in gp120 trimers. This investigation demonstrates that nanotechnology provides a powerful tool for investigating and guiding polyvalent interactions among biological systems.

(Nanobiotechnology DOI: 10.1385/Nano:1:2:201)

Key Words: HIV-1; envelope protein gp120; self-assembled monolayers; atomic force microscopy; nanofabrication; polyvalent interactions.

Introduction

The human immunodeficiency virus type 1 (HIV-1) gains entry into host cells through the binding of its viral envelope protein gp120 with cellular receptors, such as CD4 or the glycosphingolipid galactosylceramide (GalCer) for CD4 negative cells (1–7). Based on X-ray diffraction and electron microscopy (EM) studies, it is proposed that these membrane proteins are presented at the surface of HIV as trimers (8–10). During the initial infection process, when binding to CD4 or GalCer, these trimers are likely to remain together, i.e., the initial binding of gp120 and cell receptors is trivalent in nature. Figure 1A is a schematic of the proposed trimeric complex of the HIV-1 gp120 glycoproteins (10). The V3 loop of gp120 faces the

trimer axis. Although it is still unclear which residue(s) bind to carbohydrate ligands, the separation between the two nearest-neighbor GalCer binding sites would fall between 1.3 and 9.4 nm, based on the locations of the V3 loops in each gp120 molecule. The range of trivalent binding sites is indicated by the two triangles labeled in Fig. 1. Our long-term goal is to prevent HIV adhesion to T-cells by designing and producing GalCer-based artificial structures that exhibit strong binding to viral envelope proteins. This requires understanding ligand–viral protein interactions at a molecular level. Owing to the fact that both the size and distribution of rgp120 and its receptors range from a mere fraction of a nanometer to tens of nanometers, approaches to precisely control the

Correspondence and reprint requests to:

Dr. Gang-yu Liu,
Department of Chemistry,
University of California,
One Shields Ave, Davis, CA 95616.
E-mail: liu@chem.ucdavis.edu



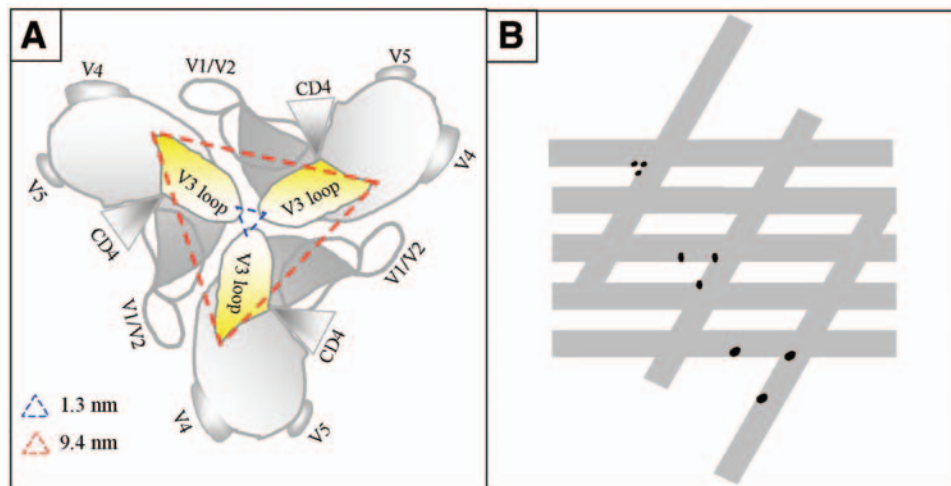


Fig. 1. (A) A schematic of the proposed model of gp120 trimers as reported in literature. **(B)** A nanostructure design: an array of crossed lines with nanometer-scaled line width. The crossed region provides binding sites for rgp120 trimers.

ligand presentation are required. The new advances in nanotechnology offer the possibility of controlling ligand distribution with nanometer precision. As the initial step toward our long-term goal, we have investigated the adsorption behavior of rgp120 proteins from solution onto various nanostructures. The key question is whether gp120 adhesion to these nanostructures exhibits any geometry dependence, as multivalent interactions would predict.

In this article, nanostructures of ligand molecules with controlled geometry and spacing within self-assembled monolayers (SAMs) are produced successfully using an atomic force microscopy (AFM)-based fabrication method known as nanografting. An example of the nanostructure design is shown in Fig. 1B, as arrays of crossed lines. This design allows monovalent and divalent binding to occur along the lines, while trivalent interactions are located at the cross-regions. If trivalent binding is favored, we expect to observe more protein adsorption at the cross-regions. *In situ* AFM imaging demonstrates selective binding of recombinant gp120 (rgp120) onto these artificially engineered ligand arrays. More important, protein molecules attach more readily at the regions that allow dimeric and trimeric binding.

Materials and Methods

Materials

The alkanethiols and thiolated carbohydrate ligands used for this investigation are summarized in Fig. 2. Normal alkanethiols, such as octanethiol and decanethiol, hereafter referred to as C8 and C10, were purchased from Aldrich with purity greater than 96% and used as received. Ethanol with a 200 proof purity was purchased from Gold Shield Chemical Co. and used as the solvent for the preparation of thiol solutions. PBS buffer was purchased from Aldrich, with a concentration of 150 mM and pH 7.3–7.4.

The carbohydrate ligand 2-[2-(2-mercaptoethoxy)ethoxy]-*N*-(galactopyranosyl-2'-methyl)acetamide (referred to as ligand Gal) was synthesized following previously reported procedures (11,12).

All materials for the synthesis of the carbohydrate ligand β -D-galactopyranosyl-2S,3R,4E-3-hydroxy-2-*N*-(11-mercapto-undecanoic acid)-sphinganine (referred to as ligand GalCer) were obtained from commercial sources and used without additional purification. All glassware for reactions under anhydrous conditions were flame-dried prior to use. Flash chromatography was performed on Silica Gel Geduran (40–63 μ m) from Merck. For TLC, silica gel 60 F₂₅₄ plates from Merck were used with detection by UV light and/or charring with AMC [ammonium molybdate (45 g) and cerium(IV) sulfate (0.9 g) in 10% H₂SO₄ (900 mL)]. ¹H NMR, COSY, HSQC, and HMBC spectra were recorded on a Bruker DRX-600 spectrometer at 25°C. Chemical shifts in ppm were referenced to CD₃OD (3.31 ppm, 49.0 ppm) as internal standard. Under an argon atmosphere, a suspension of PS-carbodiimide (Argonaut Technologies Inc., 25.1 mg, 0.034 mmol) in anhydrous CH₂Cl₂ (0.8 mL) was gently stirred for 5 min, then a solution of 11-mercapto-undecanoic acid (6.3 mg, 0.029 mmol) in anhydrous CH₂Cl₂ (0.5 mL) was added. After an additional 5 min, psychosine (10 mg, 0.022 mmol) in a 1:1 mixture of anhydrous DMF and pyridine (1 mL) was cannulated into the suspension. The reaction was allowed to stir for 18 h at ambient temperature under inert conditions. In the work-up, the resin was filtered off and washed with MeOH and CH₂Cl₂, the filtrate was concentrated and the resulting material was purified by column chromatography (eluent: CH₂Cl₂/MeOH v/v 10:1 to 5:1). The desired compound (ligand GalCer) (9.3 mg, 0.014 mmol) was obtained in 64% yield as colorless foam.

¹H NMR (600 MHz, CD₃OD) δ 0.89 (t, 3 H, J = 6.8 Hz, CH₃), 1.29 (bs, 34 H, 17 CH₂), 1.57 (bs, 4 H, CH₂-CH₂-CO,

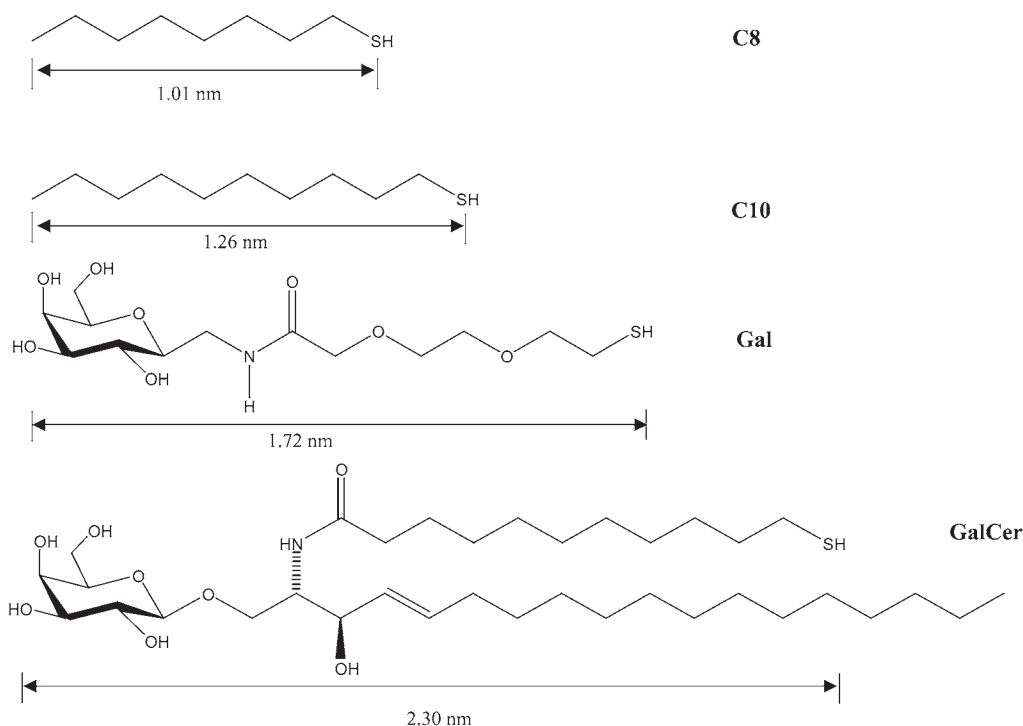


Fig. 2. Molecular structures of octanethiol, decanethiol, carbohydrate-ligand Gal, and carbohydrate-ligand GalCer used in this investigation. The estimated length from the head to the terminal groups is also indicated.

$\text{CH}_2\text{-CH}_2\text{-SH}$), 2.02 (m, 2 H, $\text{CH}_2\text{-CH=CH}$), 2.17 (t, 1H, $J = 7.6$ Hz, $\text{CH}_2\text{-CONH}$), 2.48 (t, 1 H, $J = 7.1$ Hz, $\text{CH}_2\text{-SH}$), 3.47 (dd, 1 H, $J_{2,3} = 9.7$ Hz, $J_{3,4} = 3.1$ Hz, H-3), 3.51 (m, 1 H, H-5), 3.53 (dd, 1 H, $J_{1,2} = 7.6$ Hz, $J_{2,3} = 9.7$ Hz, H-2), 3.59 (dd, 1 H, $J_{1',1''} = 10.1$ Hz, $J_{1',2} = 3.1$ Hz, H-1''), 3.71 (app dd, 2 H, $J_{6,6'} = 11.3$ Hz, $J_{5,6} = 5.2$ Hz, H-6), 3.76 (app dd, 2 H, $J_{6,6'} = 11.3$ Hz, $J_{5,6'} = 7.1$ Hz, H-6'), 3.82 (dd, 1H, $J_{3,4} = 3.1$ Hz, $J_{4,5} = 1.1$ Hz, H-4), 3.98 (m, 1 H, H-2'), 4.08 (t, $J_{2,3} = J_{3,4} = 8.0$ Hz, H-3'), 4.16 (dd, 1 H, $J_{1',1''} = 10.1$ Hz, $J_{1',2} = 4.7$ Hz, H-1'), 4.21 (d, $J_{1,2} = 7.6$ Hz, H-1), 5.45 (m, 1 H, H-4'), 5.68 (m, 1 H, H-5'). ^{13}C NMR (HSQC, HMBC, 150 MHz, CD_3OD) δ 13.55 (CH_3), 22.81 ($\text{CH}_2\text{-CH=CH}$), 28.51, 29.24, 29.51, 29.81, 30.12, 32.28 (17 CH_2), 24.01 ($\text{CH}_2\text{-SH}$), 26.21 ($\text{CH}_2\text{-CH}_2\text{-SH}$), 34.45 ($\text{CH}_2\text{-CH}_2\text{-CONH}$), 36.58 ($\text{CH}_2\text{-CONH}$), 53.82 (C-2'), 61.55 (C-6), 69.11 (C-1'), 69.62 (C-4), 71.89 (C-2), 72.11 (C-3'), 73.89 (C-3), 75.91 (C-5), 104.21 (C-1), 129.85 (C-5'), 133.12 (C-4'), 173.94 (NHCO).

Preparation of Self-Assembled Monolayers

The SAMs used for this study follow established procedures for the formation of monolayers from the solution phase (13,14). Gold (Alfa Aesar, 99.99%) was deposited in a high-vacuum evaporator (Denton Vacuum, Model DV502-A) at a base pressure below 2×10^{-6} Torr onto freshly cleaved mica substrates (clear ruby muscovite, Mica New York Corp.). The mica was preheated to 350°C before deposition using two quartz lamps, which are mounted behind the mica to facilitate the formation of large Au(111) terraces (15–19).

Typical evaporation rates were 3 \AA/s and the thickness of the gold films ranged from 1500 to 2000 \AA . After the evaporation, the gold thin films were annealed at 365°C under vacuum for 30 min and allowed to cool to room temperature. The gold films were transferred into the designated thiol solutions within 15 min after removal from the high vacuum chamber to avoid contamination. The thiols used for this study are summarized in Fig. 2, where alkanethiols form SAM matrices and the ligand Gal and GalCer solutions are used for nanografting, as described below. High-quality SAMs are formed upon soaking in 1 mM thiol/ethanol solutions for over 24 h (20–22).

Preparation of Protein Solutions

Recombinant gp120 (HIV-1 IIIB) was purchased from Trinity Biotech with a purity of more than 90%. The HIV-1 gp120 monoclonal antibody IgG1b12 was provided by McKesson BioServices Corporation under an NIH AIDS Research and Reference Reagent Program. Both rgp120 and IgG1b12 were diluted in PBS buffer to the desired concentrations of 25 and 80 $\mu\text{g/mL}$, respectively, before AFM experiments.

Atomic Force Microscopy

The atomic force microscope incorporates a home-constructed, deflection-type scanning head that exhibits high mechanical stability. The instrument allows simultaneous acquisition of multiple images such as topography, friction

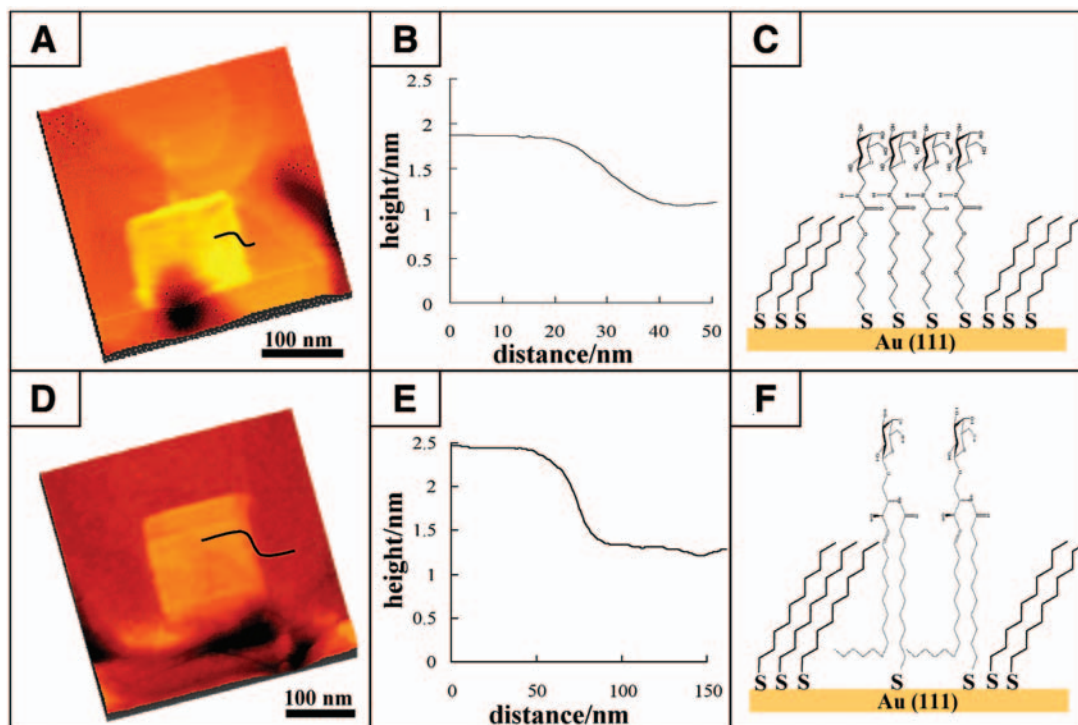


Fig. 3. Fabrication of ligand nanostructures using nanografting. **(A)** A $300 \text{ nm} \times 300 \text{ nm}$ AFM topographic image including a $130 \text{ nm} \times 110 \text{ nm}$ rectangle of ligand Gal in a C8 matrix SAM. **(B)** Cursor profile corresponding to the line in **(A)**. **(C)** Side view of a proposed packing model of Gal molecules in the pattern. **(D)** A $400 \text{ nm} \times 400 \text{ nm}$ AFM topographic image including a $150 \text{ nm} \times 150 \text{ nm}$ square of ligand GalCer in a C10 matrix SAM. **(E)** Cursor profile corresponding to the line in **(D)**. **(F)** Side view of a proposed packing model of GalCer molecules in the pattern.

force, and elasticity. The scanner was controlled by an AFM 100 preamplifier and the STM 1000 electronics (RHK Technology, Inc. Troy, MI). The AFM scanner was calibrated laterally via the known periodicity of a mica (0001) surface (0.518 nm) and vertically using the single atomic step of a gold (111) surface (0.235 nm). Sharpened Si_3N_4 microlevers (Veeco Metrology Group, Santa Barbara, CA) with a force constant of 0.1 N/m were used for AFM imaging. Images were acquired using contact mode in liquid media.

Nanografting

Nanografting is an AFM-based fabrication method developed in the Liu laboratory (23–25). A brief and general description of nanografting is as follows. A SAM matrix is imaged under low force, from which the fabrication location is chosen. The imaging force is then increased above the displacement threshold to remove thiols from the gold. Because the matrix SAM and AFM cantilever are both immersed in a solution containing the desired thiolated carbohydrate ligands, the ligand molecules attach to the newly exposed gold areas following the displacement trajectory. Because the tip-surface contact is at the molecular level, the nanostructures of ligand molecules can be produced with molecular precision (23,26). We were able to produce rectangular nanodots as small as $2 \text{ nm} \times 4 \text{ nm}$ and lines as narrow as 10 nm in width (23,26,27).

The concentrations of both ligand solutions range from 0.06 to 1.0 mM.

Results

Qualitative Evidence of Polyvalent Binding Between *rgp20* and Nanostructures of Carbohydrate Ligands

Using nanografting, nanostructures of carbohydrate ligands, such as thiolated Gal and GalCer, have been produced. Figure 3 shows two nanostructures, a $130 \text{ nm} \times 110 \text{ nm}$ ligand Gal pattern inlaid in a C8 SAM (Fig. 3A), and a $150 \text{ nm} \times 150 \text{ nm}$ GalCer-terminated thiol inlaid in a C10 SAM (Fig. 3D). The apparent heights of the two nanostructures measured from cursor profiles (Fig. 3B,E) are 0.75 and 1.15 nm above the surrounding SAM, respectively. These apparent heights of Gal- and GalCer-terminated thiols suggest an upright configuration, as schematically shown in Fig. 3C,E. The configurational difference between alkanethiols and thiolated carbohydrate ligands in SAMs is likely due to the structural differences of the molecules. As shown in Fig. 2, thiolated Gal molecules incorporate an ethylene glycol backbone with a bulky carbohydrate headgroup, while thiolated GalCer has a hydrocarbon chain. These structural differences between alkanethiols and carbohydrate ligands impact the interchain

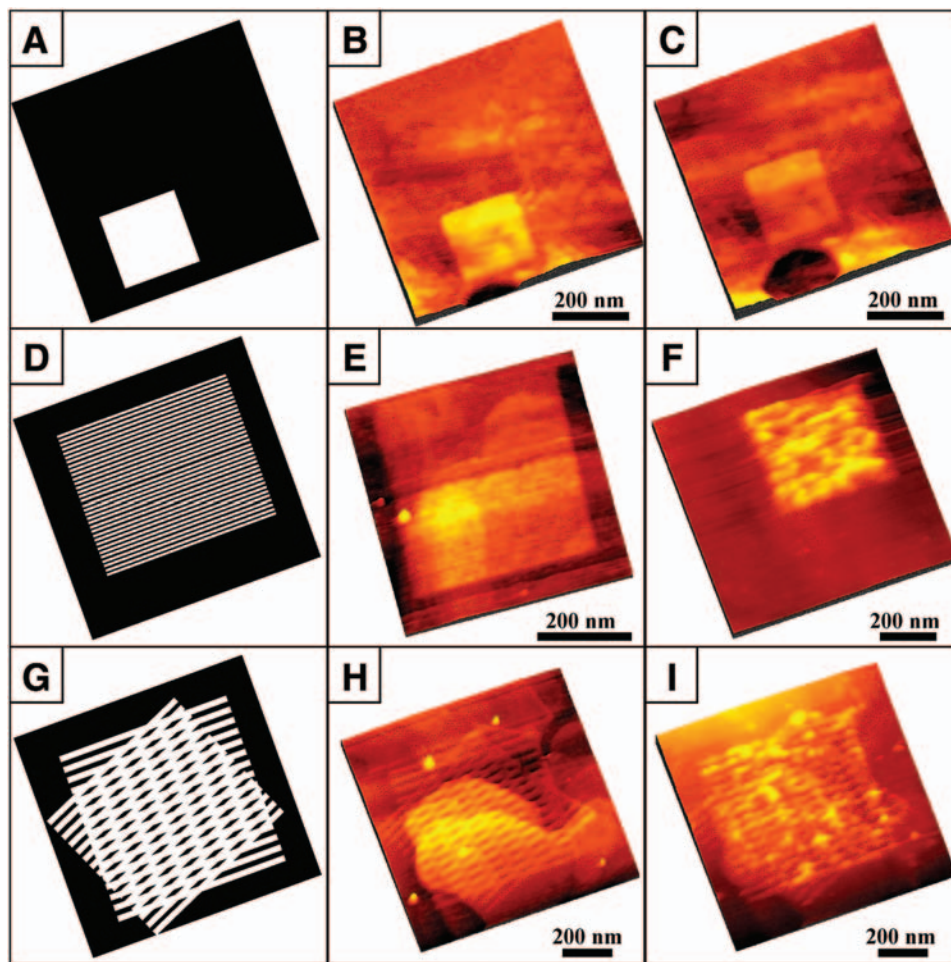


Fig. 4. The geometry dependence of rgp120 adsorption on ligand nanostructures. **(A)** The schematic of a 200 nm \times 200 nm square inlaid in C8 SAM. **(B)** AFM topograph of a 200 nm \times 200 nm GalCer square pattern produced using nanografting: 256 lines per frame, scanning speed 500 nm/s. **(C)** Same area as **(B)** after 60 min immersion in a 25 μ g/mL rgp120 solution. **(D)** The schematic of an array of lines with designed separation. **(E)** AFM topograph of an array of 32 lines covering 400 nm \times 400 nm area, produced using nanografting: 32 lines per frame under a shaving speed of 500 nm/s. **(F)** Same area as **(E)** after 60 min immersion in 25 μ g/mL rgp120 solution. **(G)** A logo of an array of crossed lines with designed line width, separation, and angle. **(H)** AFM topograph of two arrays of lines crossing in space. Each line array contains 16 lines homogeneously distributed within 600 nm \times 600 nm areas, and the two arrays are rotated 30° with respect to each other. Nanografting conditions are 16 lines per frame with a shaving speed of 500 nm/s. **(I)** Same area as **(H)** after 60 min immersion in 25 μ g/mL rgp120 solution followed by rinsing with 1% Tween 20 solution.

interactions, and thus their final configurations within SAMs. Molecules within the nanostructure are closely packed and therefore exhibit only small deformation under tip pressure.

Figure 4 shows three representative examples of nanostructures of GalCer-terminated ligands and the subsequent gp120 binding. The designed geometry of each experiment is shown on the left column, while the actual AFM topographs of the surface are revealed in the center column. In Fig. 4B, a 200 nm \times 200 nm square of ligands within which GalCer molecules are closely packed was produced by nanografting. This GalCer nanostructure provides a high density of binding site for rgp120, where chains are closely packed. In the surrounding area of the C8 SAM, a very low density of GalCer-ligand domains may be found, mostly single molecules, due to the

exchange between surface alkanethiols and solution-phase thiolated GalCer. Upon injection of a 25 μ g/mL rgp120 solution protein molecules adsorb indiscriminately on all surfaces within 30 min. Figure 4C was acquired 90 min after the immersion in rgp120 solution followed by a thorough rinsing using 1% Tween 20 (a mild detergent) and a PBS buffer. Physisorbed proteins were washed away by the detergent solution, and the remaining rgp120 molecules should be those immobilized via binding with GalCer ligands. There were very few immobilized proteins visible in Fig. 4C. The lack of protein adsorption is attributed to the steric hindrance in the high-density ligand nanostructures. Each GalCer group is surrounded by neighboring molecules and thus is hardly accessible by the V3 loop of rgp120.

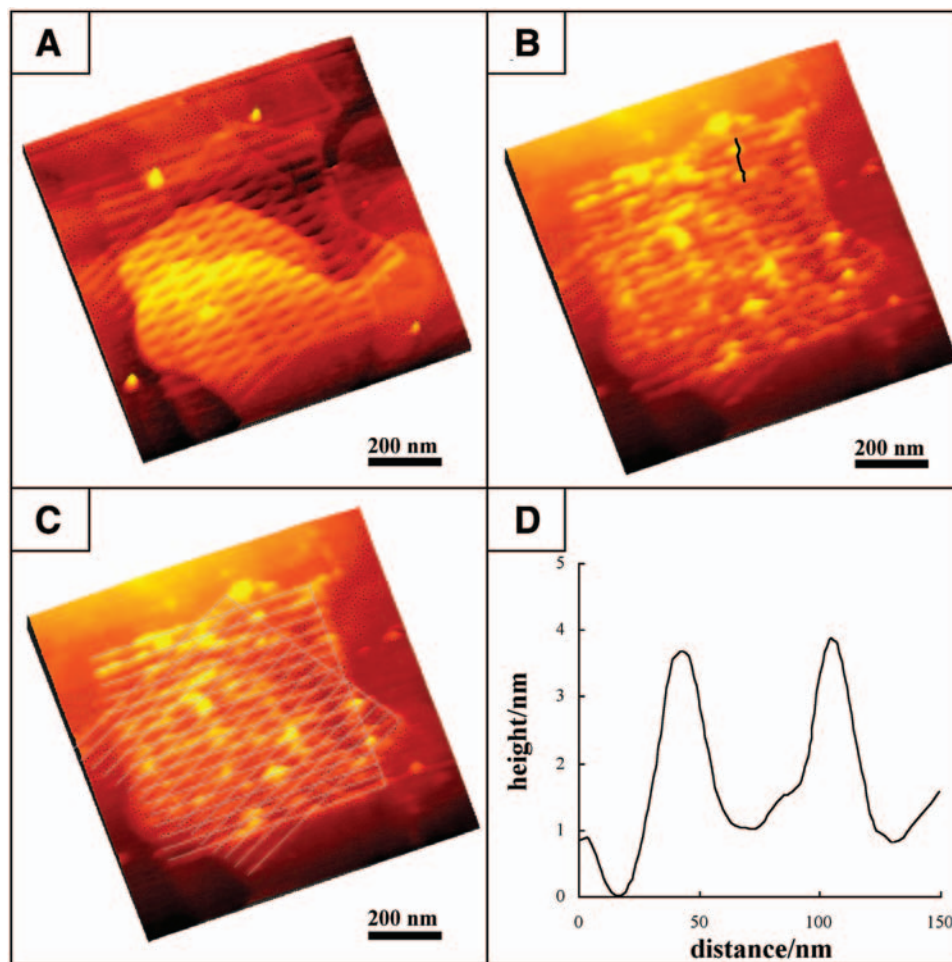


Fig. 5. A high-resolution view of the adsorption of rgp120 on a GalCer nanostructure containing crossed lines. **(A)** A $900 \text{ nm} \times 900 \text{ nm}$ AFM topographic image showing an array of crossed lines with a 30° rotation. Each line contains GalCer thiols with a line width of 12 nm, produced using two sequences of nanografting: 16 lines per frame, scanning speed of 500 nm/s. One large bright feature within the nanostructure and four features in the surrounding areas are due to a minute amount of contamination. **(B)** The same area imaged 60 min after injection of $25 \mu\text{g/mL}$ rgp120 followed by washing. New bright features in the nanostructure area correspond to the adsorbed protein. The proteins outside the nanostructure area are due to the exchange of thiolated GalCer with alkanethiols prior to the introduction of protein solution. **(C)** Overlay of the ligand nanostructures on the AFM topograph of **(B)** to reveal the location of rgp120 adsorption. **(D)** Cursor profile corresponding to the line indicated in **(B)**.

In contrast to nanostructures of high ligand density, arrays of lines and crossed lines allow divalent, trivalent, and polyvalent rgp120–ligand binding to occur. Figures 4E,H reveal nanolines and cross-lines of GalCer ligands, respectively. In Fig. 4E, an array of 32 lines of GalCer is produced in a $400 \text{ nm} \times 400 \text{ nm}$ area. This geometry allows for divalent binding within the lines and trivalent and multivalent binding among nearest-neighbor lines, especially with ligands at the edges of the lines where GalCer functional groups are readily accessible by rgp120. Binding of rgp120 with this line array is evident in Fig. 4F, as evidenced by the appearance of bright features upon immersion in rgp120 solutions. Shown in Fig. 4H are cross-lines of GalCer within a C8 matrix. This nanostructure contains two arrays of lines, with one array rotated 30° with respect to the other. Each array has 16 GalCer lines in

a $600 \text{ nm} \times 600 \text{ nm}$ area. This GalCer pattern allows for and guides multivalent binding at the crossed regions. The effect is visualized in Fig. 4I, where most of the bright features are located in the crossed points. Taking all the observations summarized in Fig. 4, it is inferred that rgp120 attaches to GalCer mostly via polyvalent binding.

To accurately determine the location of rgp120 binding sites within nanostructures of GalCer, high-resolution AFM images were acquired both before and after introducing rgp120 solutions. As shown in Fig. 5, rgp120 adsorption is evident by the appearance of bright features, each of which represents immobilized rgp120 molecules. Overlaying the nanostructure in Fig. 5A onto 5B allows for molecular-level identification of rgp120 binding sites. As revealed in Fig. 5C, most protein molecules are found at the intersections of the

lines in this nanostructure, where the probability of multivalent, especially trivalent, binding is the highest. Figure 5D is the cursor profile corresponding to the line indicated in Fig. 5B, from which the apparent heights are extracted to be 2.5 and 2.7 nm, respectively. The crystal structure at 0.25 nm resolution revealed that the gp120 core folds into a heart-shaped globular structure with dimensions of 5 nm × 5 nm × 2.5 nm (28). Thus the observed height is consistent with the immobilization of rp120 with its main axis parallel to the surface. The variation in the contrast of the protein molecules reveals the coexistence of monomer, dimers, and trimers of rp120, with a couple of large aggregates. The results shown in Fig. 5 lead to a significant conclusion, i.e., rather than random adsorption on the ligands, rp120 molecules preferentially bind at the crossed line regions of this nanostructure, where the probability of trivalent binding is the highest. Nanotechnology in this case provides an alternative confirmation of the multivalent nature of rp120–ligand interactions, and suggests a new platform to control such binding, via the geometry of the nanostructures. The robustness of the trivalent interactions is verified using other crossed line arrays with various angles of crossing—15°, 30°, 45°, and 90°. All experiments indicate that rp120 prefers the cross-point regions as the binding sites, where the details vary depending upon the locations of ligands at the cross-line areas.

Geometry-Dependence of the *rgp120* Binding to Carbohydrate Ligands

We anticipate strong separation dependence for *rgp120* binding on arrays of parallel nanolines of carbohydrate ligand if the interaction between *rgp120* and GalCer is polyvalent. Figure 6 shows the adsorption of *rgp120* onto various arrays of nanolines. In the case of 16 lines covering the area of 400 nm × 400 nm as shown in Fig. 6B, the line width is 12.4 nm, as measured from the full-width at half-maximum (FWHM) of the cursor profile (see Fig. 6E). Nearest-neighbor lines are separated by about 25.0 nm, center-to-center, close to the theoretical value of $400/(16-1) = 26.7$ nm. Owing to the finite width of the lines, the edge-to-edge separation is about 12.7 ± 1.0 nm, as also determined from the image and cursor profiles. Upon soaking in a 25 µg/mL *rgp120* solution, protein adsorption did occur, covering 20% of the nanostructure area. The edge-to-edge separation is wider than the trimer binding range, 1.3 to 9.4 nm, thus only divalent and a small amount of trivalent binding could occur, owing to the line position deformation during fabrication and chain flexibility. Therefore, the coverage of protein is not optimal. Decreasing the line separation should facilitate the trimeric binding of *rgp120* onto ligands. This trend is demonstrated in Fig. 6G, where the line density is doubled, 32-lines per frame. The center-to-center separation between adjacent lines is 12.5 nm, consistent with the theoretical value [$400/(32-1) = 12.9$ nm]. More *rgp120* binding did occur, as shown in Fig. 6I, with most of the proteins located at the edges of these lines. The edge-to-edge distance in this case is 4.8 nm, falling in the

range of trivalent interactions as proposed in Fig. 1. The nanoengineering approach clearly reveals the importance of geometry parameters in multivalent binding.

Bioactivity Evaluation of Adsorbed *rgp120* on Ligand Nanostructures

Because it is difficult to perform a bioassay on such a minute amount of *rgp120* molecules, one must evaluate the bioactivity of nanostructures of *rgp120 in situ*. The *rgp120* is composed of five constant regions (C1–C5) interspersed with five variable regions (V1–V5) (29,30). It has been revealed that the binding site of the protein for its specific interaction with GalCer is in the V3 region (31,32). Most of the HIV-neutralizing antibodies target the V3 loop of gp120. These antibodies are not good candidates for nanobioassays because the epitope in gp120 for these antibodies is blocked after binding with GalCer. A more viable candidate would be the CD4 binding site. X-ray diffraction studies have shown that the binding site of *rgp120* to the CD4 receptor is not close to the V3 loop of the protein. Therefore, antibodies targeting CD4 binding sites, such as IgG1b12, may be utilized to recognize the *rgp120* molecules upon immobilization onto nanostructures of ligands.

Figure 7 shows the *in situ* AFM topographic images of nanostructure, *rgp120* binding, and anti-*rgp120* antibody recognition processes. Figure 7A shows the two constructed ligand nanostructures prior to protein injection. Upon soaking in 25 µg/mL *rgp120* solution for 60 min, there is no observable binding of *rgp120* on the square GalCer pattern (Fig. 7B), in which the ligands are closely packed. In the array of crossed lines of GalCer, the binding *rgp120* molecules is readily visible. Upon removal of *rgp120* solution and washing with 1% Tween 20 solution and PBS buffer, a solution containing the *rgp120* monoclonal antibody, IgG1b12, was then injected. Figure 7C is the AFM topography acquired 60 min after soaking in antibody solution, where the morphological change in the nanostructure region is clearly visualized in the AFM topograph. The antibody-recognition process is further confirmed using a combined cursor profile shown in Fig. 7D, where the height increase of 4.0 ± 1.0 nm indicates the binding of antibody to *rgp120* nanostructures. Antibodies typically have a Y-shaped structure with dimensions of 4.5 nm × 8.0 nm × 14.5 nm. Therefore, the measured height increase of 4 nm suggests that most of the IgG1b12 lay down on the surface of the nanostructures under the applied load of AFM tips. This recognition process demonstrates the activity of *rgp120* is maintained upon immobilization onto engineered nanostructures.

Discussion

A series of nanostructures were designed and produced to investigate the binding between *rgp120* and GalCer ligands. In the geometry of cross-lines, *rgp120* molecules were found to prefer the cross sections of GalCer lines. These locations provide binding sites for *rgp120* trimers. Therefore,

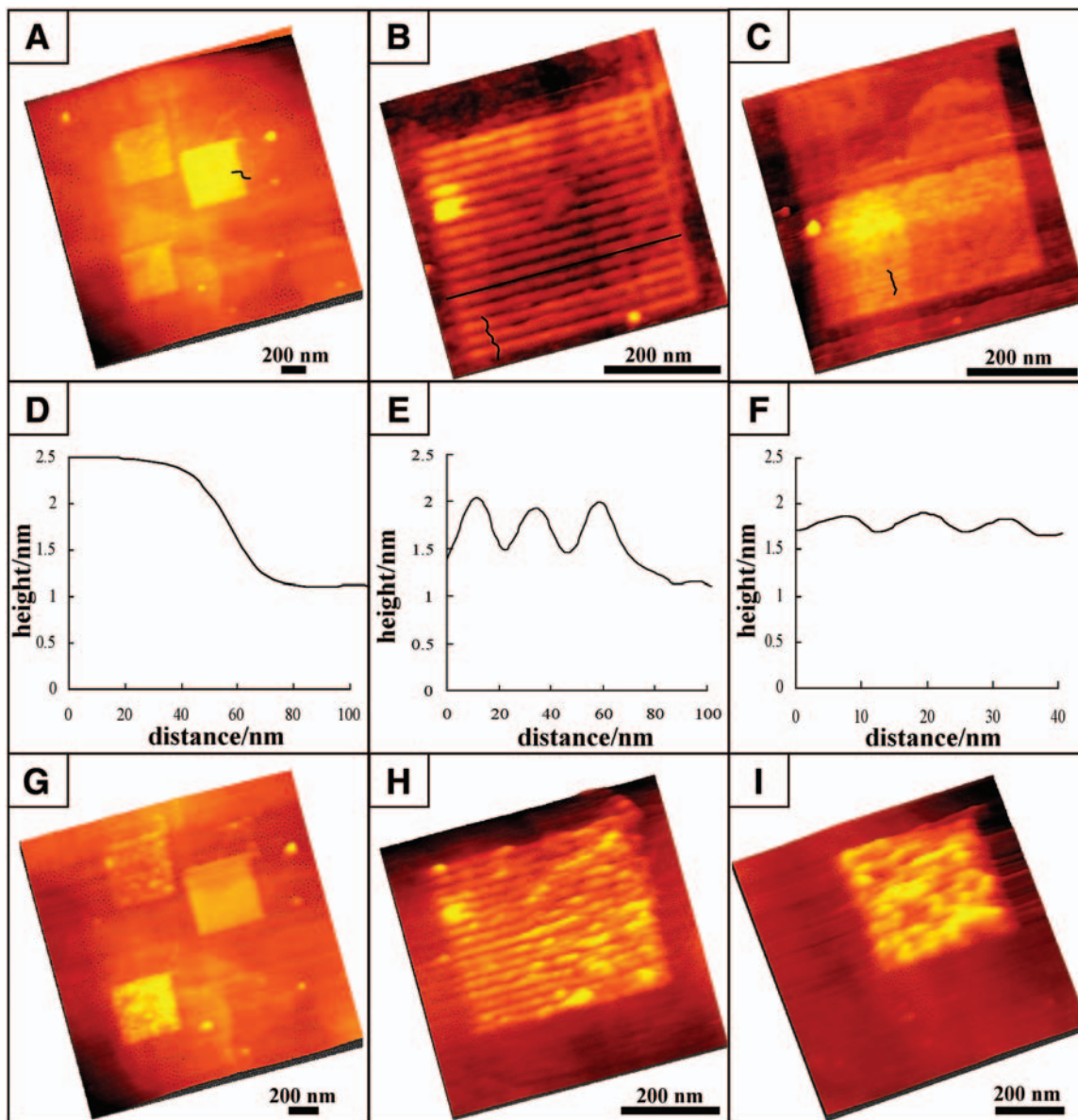


Fig. 6. Dependence of the rgp120 adsorption on the separation of lines in arrays of ligand lines. **(A)** An 1800 nm \times 1800 nm AFM topographic image containing three GalCer patterns in a C8 matrix. From top to bottom, the line arrays are fabricated by 16, 256, and 32 lines per frame, respectively, under 40 nN shaving force. **(B)** A zoom-in view of the 16-line GalCer pattern. **(C)** A zoom-in image of the 32-line ligand nanostructure. **(D)**, **(E)**, and **(F)** are cursor profiles corresponding to the three lines indicated in **(A)**, **(B)**, and **(C)**, respectively. **(G)** A 1500 nm \times 1500 nm AFM topographic image containing the three nanostructures after 60 min soaking in a 200 nM rgp120 solution. **(H)** A zoom-in view of the 16-line pattern after protein adsorption. **(I)** A zoom-in image of the 32-line nanostructures upon attachment of rgp120.

the location-dependent behavior suggests that gp120–GalCer interactions are polyvalent in nature in most cases. This observation is a direct confirmation of the polyvalent model proposed in our previous studies, in which gold nanoparticles with an average diameter of 2 nm and coated with ligand Gal show a stronger binding to rgp120 molecules than do single biotinylated GalCer molecules (12). Other evidence comes from electron microscopy studies of HIV viruses, where the viral surface is found to be decorated with spikes (33–35). These spikes are the oligomer, most likely a trimer, of gp120–gp41

complex expressed on the viral surface. The diameter of each spike observed is about 14 nm. Those surface morphologies of HIV virus have also been revealed by AFM imaging. The average size of the spikes is 20 nm in diameter (36). The enlargement of the lateral size from AFM studies can be attributed to the tip-induced convolution (37–39). In addition, the protein IgG with dimensions of 4.0 nm \times 8.0 nm \times 14.5 nm, which is close to the gp120 trimer in size, has been imaged by AFM in our previous studies (40). The measured size of the single protein has a height ranging from 2 to 4 nm and

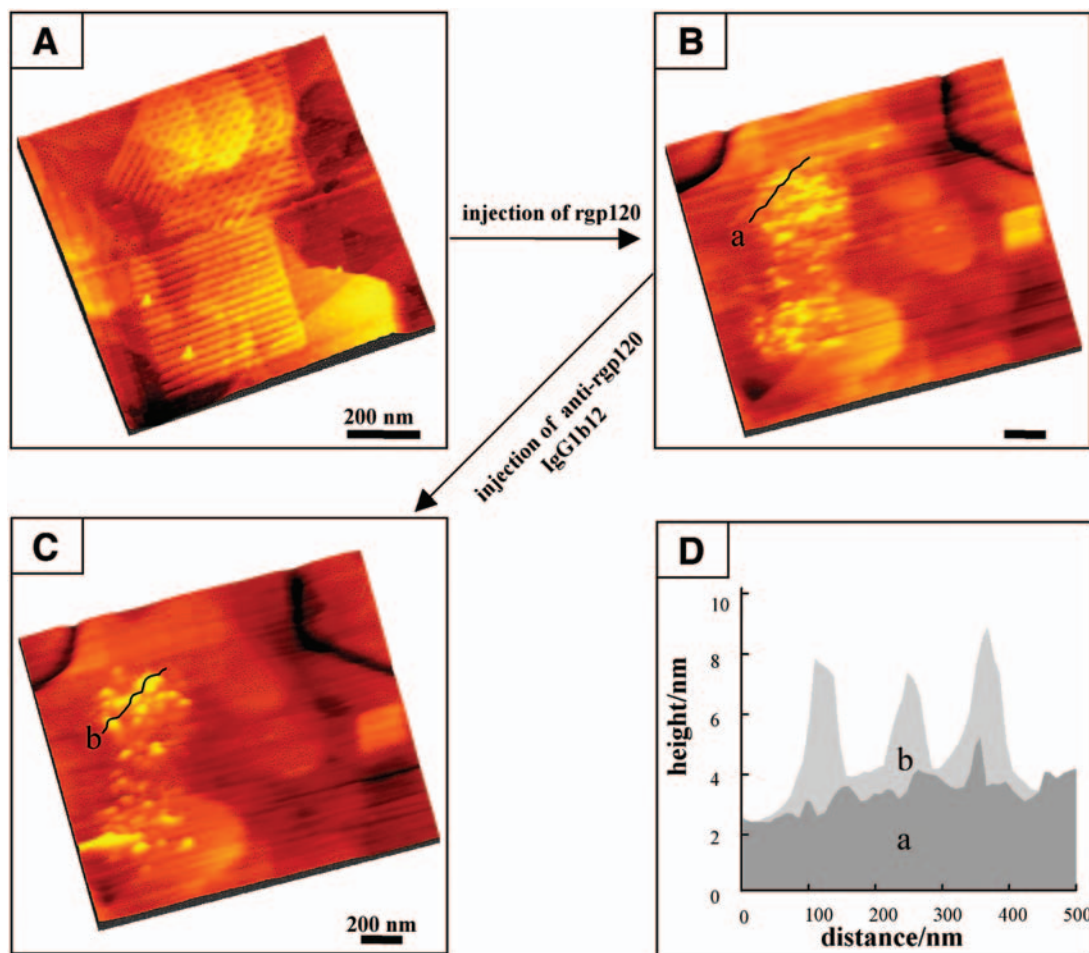


Fig. 7. Test of the bioactivity of rgp120 upon adsorption on ligand nanostructures. **(A)** An $850 \text{ nm} \times 850 \text{ nm}$ AFM topographic image revealing two GalCer nanostructures in a C10 SAM. The top pattern contains two 16-line arrays rotated 45° with respect to each other. Each array covers a $400 \text{ nm} \times 400 \text{ nm}$ area. The bottom pattern is an array containing 16 lines in a $400 \text{ nm} \times 400 \text{ nm}$ area. **(B)** AFM topographic image acquired 60 min after the injection of $25 \text{ }\mu\text{g/mL}$ rgp120. The $200 \text{ nm} \times 200 \text{ nm}$ square was produced at 500 nm/s and 28 lines per frame. **(C)** The same area as **(B)** after the subsequent injection of $80 \text{ }\mu\text{g/mL}$ IgG1b12, an anti-rgp120 monoclonal antibody. **(D)** A combined cursor profile as indicated in **(B)** and **(C)** reveals the increase in heights, which is an indication of antibody recognition.

lateral dimensions ranging from 14 to 20 nm. Therefore, our observed bright features, 20 nm in lateral dimension, at the crossed regions are consistent with the gp120 trimers observed in the actual viruses. Because artificial structures and isolated proteins are used, single-protein adsorption and large aggregates are occasionally visible.

Arrays of parallel lines are used to determine the optimal line separation for gp120 binding. Our systematic studies suggest that the optimal protein immobilization is achieved when the edge-to-edge separation falls in the range of the three V3 loops in gp120 trimer, i.e., 1.3–9.4 nm. In fact, our results suggest a separation of 4.8 nm is the optimal binding geometry. Higher-resolution studies are in progress to reveal the actual binding site of GalCer in the V3 loop of gp120.

Acknowledgments

We thank Drs. S. Kauzlarich, M. Longo, S. Dandekar, and Ms. S. Leigh at UC Davis for many helpful discussions. This

work was supported by the University of California, Davis, National Science Foundation through a NIRT grant CHE 0210807 and a seed fund from CPIMA program (MRSEC grant to Stanford University). Additional funding is provided by NSF CRIF program (CHE-9808183), NSF OSTI 97-24412 and NIH Grant RR11973. J.J. Yu thanks Tyco Electronics Foundation for a Graduate Fellowship in Functional Materials. The following reagent was obtained through the NIH AIDS Research and Reference Reagent Program, Division of AIDS, NIAID, NIH: HIV-1 gp120 Monoclonal (IgG1 b12), cat. no. 2640 from Drs. D. Burton and P. Parren.

References

1. Yahi, N., Baghdiguian, S., Moreau, H., and Fantini, J. (1992), *J. Virology* **66**, 4848–4854.
2. Harouse, J. M., Kunsch, C., Hartle, H. T., et al. (1989), *J. Virology* **63**, 2527–2533.

3. Harouse, J. M., Bhat, S., Spitalnik, S. L., et al. (1991), *Science* **253**, 320–323.
4. McAlarney, T., Apostolski, S., Lederman, S., and Latov, N. (1994), *J. Neurosci. Res.* **37**, 453–460.
5. Brogi, A., Presentini, R., Solazzo, D., Piomboni, P., and Constantino-Ceccarini, E. (1996), *Aids Res. Hum. Retroviruses* **12**, 483–489.
6. Brogi, A., Presentini, R., Piomboni, P., et al. (1995), *J. Submicrosc. Cytol. Pathol.* **27**, 565–571.
7. Bhat, S., Spitalnik, S. L., Gonzalezscarano, F., and Silberberg, D. H. (1991), *Proc. Natl. Acad. Sci. USA* **88**, 7131–7134.
8. Earl, P. L., Doms, R. W., and Moss, B. (1990), *Proc. Natl. Acad. Sci. USA* **87**, 648–652.
9. Center, R. J., Leapman, R. D., Lebowitz, J., Arthur, L. O., Earl, P. L., and Moss, B. (2002), *J. Virology* **76**, 7863–7867.
10. Wyatt, R., Kwong, P. D., Desjardins, E., et al. (1998), *Nature* **393**, 705–711.
11. McReynolds, K. D., Hadd, M. J., and Gervay-Hague, J. (1999), *Bioconjug. Chem.* **10**, 1021–1031.
12. Nolting, B., Yu, J. J., Liu, G. Y., Cho, S. J., Kauzlarich, S., and Gervay-Hague, J. (2003), *Langmuir* **19**, 6465–6473.
13. Nuzzo, R. G. and Allara, D. L. (1983), *J. Am. Chem. Soc.* **105**, 4481–4483.
14. Nuzzo, R. G., Fusco, F. A., and Allara, D. L. (1987), *J. Am. Chem. Soc.* **109**, 2358–2368.
15. Hegner, M., Wagner, P., and Semenza, G. (1993), *Surf. Sci.* **291**, 39–46.
16. Wagner, P., Hegner, M., Guntherodt, H. J., and Semenza, G. (1995), *Langmuir* **11**, 3867–3875.
17. Chidsey, C. E. D., Loiacono, D. N., Sleator, T., and Nakahara, S. (1988), *Surf. Sci.* **200**, 45–66.
18. Woll, C., Chiang, S., Wilson, R. J., and Lippel, P. H. (1989), *Phys. Rev. B* **39**, 7988–7991.
19. Lang, C. A., Dovek, M. M., Nogami, J., and Quate, C. F. (1989), *Surf. Sci.* **224**, L947–L955.
20. Poirier, G. E. and Pylant, E. D. (1996), *Science* **272**, 1145–1148.
21. Poirier, G. E. (1997), *Chem. Rev.* **97**, 1117–1127.
22. Qian, Y. L., Yang, G. H., Yu, J. J., Jung, T. A., and Liu, G. Y. (2003), *Langmuir* **19**, 6056–6065.
23. Xu, S. and Liu, G. Y. (1997), *Langmuir* **13**, 127–129.
24. Xu, S. and Liu, G. Y. (1999), *Scanning* **21**, 71–71.
25. Xu, S., Miller, S., Laibinis, P. E., and Liu, G. Y. (1999), *Langmuir* **15**, 7244–7251.
26. Liu, G. Y., Xu, S., and Qian, Y. L. (2000), *Acc. Chem. Res.* **33**, 457–466.
27. Amro, N. A., Xu, S., and Liu, G. Y. (2000), *Langmuir* **16**, 3006–3009.
28. Kwong, P. D., Wyatt, R., Robinson, J., Sweet, R. W., Sodroski, J., and Hendrickson, W. A. (1998), *Nature* **393**, 648–659.
29. Starcich, B. R., Hahn, B. H., Shaw, G. M., et al. (1986), *Cell* **45**, 637–648.
30. Leonard, C. K., Spellman, M. W., Riddle, L., Harris, R. J., Thomas, J. N., and Gregory, T. J. (1990), *J. Biol. Chem.* **265**, 10,373–10,382.
31. Cook, D. G., Fantini, J., Spitalnik, S. L., and Gonzalezscarano, F. (1994), *Virology* **201**, 206–214.
32. Fantini, J., Hammache, D., Delezay, O., et al. (1997), *J. Biol. Chem.* **272**, 7245–7252.
33. Gelderblom, H. R., Hausmann, E. H. S., Ozel, M., Pauli, G., and Koch, M. A. (1987), *Virology* **156**, 171–176.
34. Ozel, M., Pauli, G., and Gelderblom, H. R. (1988), *Arch. Virology* **100**, 255–266.
35. Nermut, M. V., Grief, C., Hashmi, S., and Hockley, D. J. (1993), *Aids Res. Hum. Retroviruses* **9**, 929–938.
36. Kuznetsov, Y. G., Victoria, J. G., Robinson, W. E., and McPherson, A. (2003), *J. Virology* **77**, 11,896–11,909.
37. Allen, M. J., Hud, N. V., Balooch, M., Tench, R. J., Siekhaus, W. J., and Balhorn, R. (1992), *Ultramicroscopy* **42**, 1095–1100.
38. Markiewicz, P. and Goh, M. C. (1995), *J. Vacuum Sci. Tech. B* **13**, 1115–1118.
39. Xu, S., Amro, N. A., and Liu, G. Y. (2001), *Appl. Surf. Sci.* **175**, 649–655.
40. Wadu-Mesthrige, K., Amro, N. A., Garno, J. C., Xu, S., and Liu, G. Y. (2001), *Biophys. J.* **80**, 1891–1899.